A&A 558, L7 (2013)
DOI: 10.1051/0004-6361/201322432

Astronomy & Astrophysics

Letter to the Editor

OTS 44: Disk and accretion at the planetary border[⋆,⋆⋆]

V. Joergens[1,2], M. Bonnefoy[1], Y. Liu[3,4], A. Bayo[1,5], S. Wolf[4], G. Chauvin[6], and P. Rojo[7]

[1] Max-Planck-Institut für Astronomie, Königstuhl 17, 69117 Heidelberg, Germany
e-mail: viki@mpia.de
[2] Universität Heidelberg, Zentrum für Astronomie, Inst. für Theor. Astrophysik, Albert-Ueberle-Str. 2, 69120 Heidelberg, Germany
[3] Purple Mountain Observatory & Key Laboratory for Radio Astronomy, Chinese Academy of Sciences, 210008 Nanjing, PR China
[4] Institut für Theoretische Physik und Astrophysik, Universität Kiel, Leibnizstr. 15, 24118 Kiel, Germany
[5] European Southern Observatory, Alonso de Córdova 3107, Vitacura, 19001 Casilla, Santiago, Chile
[6] Inst. of Planetology & Astrophysics Grenoble, 414 rue de la Piscine, Domaine universitaire, 38400 Saint-Martin d'Hères, France
[7] Departamento de Astronomia, Universidad de Chile, 36-D Casilla, Santiago, Chile

Received 2 August 2013 / Accepted 1 October 2013

ABSTRACT

We discover that the very low-mass brown dwarf OTS 44 ($M9.5$, $\sim$12 $M_{\rm Jup}$) has significant accretion and a substantial disk, which demonstrates that the processes that accompany canonical star formation occur down to a central mass of a few Jupiter masses. We discover in VLT/SINFONI spectra that OTS 44 has strong, broad, and variable Paβ emission that is evidence for active accretion at the planetary border. We also detect strong Hα emission of OTS 44 in a literature spectrum and determine an Hα EW of -141 Å, which indicates active accretion. Both the Paβ and Hα emission lines have broad profiles with wings extending to velocities of about $\pm$200 km s^{-1}. We determine the mass accretion rate of OTS 44 based on Hα to 7.6 $\times$ 10^{-12} $M_\odot$ yr^{-1}. This result shows that OTS 44 has a relatively high mass-accretion rate considering its small central mass. This mass rate is nevertheless consistent with the general decreasing trend found for stars of several solar masses down to brown dwarfs. Furthermore, we determine the properties of the disk surrounding OTS 44 through radiative transfer modeling of flux measurement from the optical to the far-IR (*Herschel*) by applying a Bayesian analysis. We find that OTS 44 has a highly flared disk ($\beta > 1.2$) with a mass of $9.1^{+1.7}_{-5.5} \times 10^{-5}$ $M_\odot$, i.e. $\sim$0.1 $M_{\rm Jup}$ or 30 $M_{\rm Earth}$. We show that the ratio of the disk-to-central-mass of about 10^{-2} found for objects between 0.03 $M_\odot$ and 14 $M_\odot$ is also valid for OTS 44 at a mass of $\sim$0.01 $M_\odot$. Our observations are in line with an isolated star-like mode of the formation of brown dwarfs down to 0.01 $M_\odot$.

Key words. brown dwarfs – stars: pre-main sequence – circumstellar matter – accretion, accretion disks – stars: formation – stars: individual: OTS 44

1. Introduction

One of the main open questions in the theory of star formation is: How do brown dwarfs form? A high-density phase is necessary for the gravitational fragmentation to create very small Jeans-unstable cores. Proposed scenarios to prevent a substellar core in a dense environment from accreting to stellar mass are (i) ejection of the core through dynamical interactions; (ii) photo-evaporation of the gas envelope through radiation of a nearby hot star; and (iii) disk instabilities in circumstellar disks. Alternatively, brown dwarfs could form in an isolated mode by direct collapse. For example, filament collapse (e.g., Inutsuka & Miyama 1992) might form low-mass cores that experience high self-erosion in outflows and become brown dwarfs (Machida et al. 2009). A key to understanding star and brown dwarf formation is to observationally define the minimum mass that the star formation process can produce by detecting and exploring the main features characteristic of star formation, such as disks, accretion, and outflows, for very low-mass objects.

Young brown dwarfs were shown to have substantial circumstellar disks at far-IR and mm wavelengths (e.g., Harvey et al. 2012; Ricci et al. 2013). Many of these brown dwarfs were found to actively accrete material through the disk onto the central object (e.g., Rigliaco et al. 2012), and a handful of them also to drive outflows (e.g., Whelan et al. 2005; Phan-Bao et al. 2008; Bacciotti et al. 2011; Joergens et al. 2012a,b; Monin et al. 2013). Among the lowest-mass isolated objects found to harbor a disk are Cha 110913-773444 ($\sim$8 $M_{\rm Jup}$, Luhman et al. 2005a), LOri 156 ($\sim$23 $M_{\rm Jup}$, Bayo et al. 2012), and OTS 44 ($\sim$12 $M_{\rm Jup}$, Luhman et al. 2005b).

OTS 44, which is the subject of the present work, was first identified as a brown dwarf candidate in a deep near-IR imaging survey in the Chamaeleon I star-forming region (Oasa et al. 1999). It was confirmed to be a very low-mass brown dwarf of spectral-type M9.5 with an estimated mass of $\sim$15 $M_{\rm Jup}$ based on low-resolution near-IR and optical spectra (Luhman et al. 2004; Luhman 2007). Bonnefoy et al. (2013) recently confirmed in a near-IR study a mass in the planetary regime ($\sim$6$-$17 $M_{\rm Jup}$). Mid- and far-IR excess emission detected with *Spitzer* (Luhman et al. 2005b) and *Herschel* (Harvey et al. 2012) indicated that OTS 44 has a disk. We present SINFONI / VLT spectroscopy of OTS 44 that reveals strong Paschenβ emission, an analysis of Hα emission in a spectrum from Luhman (2007), and a detailed modeling of the spectral energy distribution (SED) of the disk of OTS 44 based on *Herschel* data.

2. Observations

The spectral energy distribution. To model the disk and photosphere of OTS 44, we compiled optical to far-IR flux measurements from the literature. In the optical, we use *I*-band data from

⋆ Based on observations at the Very Large Telescope of the European Southern Observatory at Paranal, Chile in program 80.C-0590(A).
⋆⋆ Appendix A is available in electronic form at http://www.aanda.org

Luhman et al. (2005b) and an R-band magnitude of 23.5 ± 0.1 (Luhman, priv. comm.). The near-IR (JHK) regime is covered by observations of 2MASS and WISE. We note that the WISE W4 photometry of OTS 44 was not used because of contamination by a bright spike. Mid-IR photometry of OTS44 was obtained by *Spitzer* using IRAC (3.6, 4.5, 5.8, 8.0 μm) and MIPS (24 μm, Luhman et al. 2008). Recently, OTS44 was observed in the far-IR (70, 160 μm) by *Herschel*/PACS (Harvey et al. 2012).

Near-infrared SINFONI integral field spectroscopy. We observed OTS 44 with the Spectrograph for INtegral Field Observations in the Near Infrared (SINFONI) at the VLT on December 14 and 21, 2007. The observations were conducted as part of a program designed to provide a library of near-IR spectra of young late-type objects (Bonnefoy et al. 2013). The instrument was operated with pre-optics and gratings enabling medium-resolution ($R = \lambda/\Delta\lambda \sim 2000$) J-band spectroscopy (1.1−1.4 μm) with a spatial sampling of 125×250 mas/pixel. We reduced the data with the SINFONI data reduction pipeline version 1.9.8 and custom routines (cf. Bonnefoy et al. 2013, for details). The pipeline reconstructs datacubes with a field of view of $1.125 \times 1.150''$ from bi-dimentional raw frames. Telluric absorptions features were calibrated and removed based on the observations of B5V stars. The wavelength calibration based on arc lamp spectra has an accuracy of about 30 km s^{-1}. A value of $V_0 = 15.2$ km s^{-1} was adopted as rest velocity of OTS 44 throughout the paper, which is the average radial velocity of T Tauri stars and brown dwarfs in Cha I (Joergens 2006).

Optical spectroscopy. An optical spectrum covering the range 0.5−1 μm with a resolution $R = 900$ was taken by Luhman (2007) with IMACS at the Magellan I telescope on January 6, 2005. This spectrum is used to analyze the Hα emission of OTS 44 and to provide an additional constraint to the photosphere model fit. We calculate the heliocentric radial velocities relative to V_0.

3. Photospheric properties of OTS 44

We find that it is not possible to fit the SED of OTS 44 when using the properties reported for this brown dwarf in the literature ($T_{\rm eff} = 2300$ K, $L_* = 0.0007\,L_\odot$, $A_V = 0$, Luhman 2007). Therefore, we performed a thorough modeling of the photosphere of OTS 44 by applying the BT-Settl models (Allard et al. 2012). These models incorporate a sophisticated treatment of photospheric dust, which is likely to affect the cool atmosphere of OTS 44. We use broad-band photometry, a narrow grid of flux points calculated from the optical spectrum (Luhman 2007), and a surface gravity log(g) of 3.5, as determined from gravity-sensitive lines (Bonnefoy et al. 2013). We derive an effective temperature of $T_{\rm eff} = 1700$ K, a luminosity of $L_* = 0.0024\,L_\odot$, and an extinction of $A_V = 2.6$ mag (Table 1). Bonnefoy et al. (2013) also found indications for a lower $T_{\rm eff}$ of OTS 44. The probability distributions of the parameter values in our modeling approach are relatively broad, which hints at a remaining discrepancy with the models. We conclude that the photospheric properties of OTS 44 may still need to be refined in the future.

4. SED modeling of the disk of OTS 44

We model the SED of OTS 44 using the radiative transfer code `MC3D` (Wolf 2003) to characterize its circumstellar environment. Because the disk parameters are strongly degenerate in the fitting procedure, we employ a passive-disk model consisting of a central substellar source surrounded by a parametrized disk.

Dust distribution in the disk. We introduce a parametrized flared disk in which dust and gas are well mixed and homogeneous throughout the system. This model has been successfully used to explain the observed SEDs of a large sample of young stars and brown dwarfs (e.g., Wolf et al. 2003; Harvey et al. 2012). For the dust in the disk we assume a density structure with a Gaussian vertical profile $\rho_{\rm dust} = \rho_0 (R_*/\varpi)^\alpha \exp(-z^2/2h^2(\varpi))$, and a power-law distribution for the surface density $\Sigma(\varpi) = \Sigma_0 (R_*/\varpi)^p$, where ϖ is the radial distance from the central star measured in the disk midplane, and $h(\varpi)$ is the scale height of the disk. The outer disk radius $R_{\rm out}$ is set to 100 AU. To allow flaring, the scale height follows the power law $h(\varpi) = h_{100}(\varpi/100\,{\rm AU})^\beta$, with the flaring exponent β describing the extent of flaring and the scale height h_{100} at $R_{\rm out}$.

Table 1. Photospheric properties of OTS 44.

	$T_{\rm eff}$ [K]	L_* [$L_\odot$]	A_V [mag]	log(g)	Reference
Set 1	2300	0.00077	0.0		Luhman (2007)
Set 2	1700	0.0024	2.6	3.5	This work

Notes. The errors for set 2 are $\Delta T_{\rm eff} = 140$ K, $\Delta L_* = 0.00054\,L_\odot$, and $A_V < 3.0$ with 90% probability. log(g) is taken from Bonnefoy et al. (2013). $T_{\rm eff}$ in set 2 agrees with the value found by Bonnefoy et al. (2013), while L_* slightly deviates between these two works.

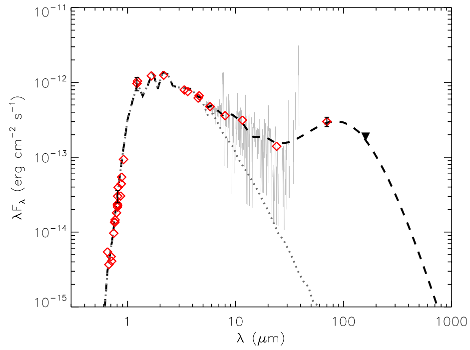

Fig. 1. SED of OTS 44. Shown are photometric measurements (red diamonds) with errors if larger than the symbol, an upper limit for the 160 μm flux (black triangle), the mid-IR *Spitzer*/IRS spectrum (light gray), the best-fit SED model (dashed line), and the input BT-Settl photosphere model (gray dotted line).

Dust properties. We consider the dust grains to be homogeneous spheres, which is a valid approximation to describe the scattering behavior as compared to a more complex description with fractal grain structures. The dust grain ensemble incorporates both astronomical silicate (62.5%) and graphite (37.5%) material. The grain size distribution is given by the standard power law $n(a) \propto a^{-3.5}$ with minimum and maximum grain sizes of 0.005 μm and 0.25 μm, respectively.

Heating sources. We consider a passive disk with only stellar irradiation, but no viscous heating (e.g., Chiang & Goldreich 1997). Radiation heating of the dust from the accretion luminosity can be neglected because $L_{\rm acc} < 0.2\%\,L_*$ (Sect. 5). For $T_{\rm eff}$ and L_* of the central source, we use the values derived here (Table 1, set 2) and $d = 162.5$ pc. As said, an SED model using the parameters from Luhman (2007; set 1 in Table 1) cannot reproduce the observations. The incident substellar spectrum is taken from the BT-Settl atmosphere database with log(g) = 3.5 (Allard et al. 2012). The radiative transfer problem is solved self-consistently considering 100 wavelengths, logarithmically distributed in the range of [0.05 μm, 2000 μm].

Fitting results. The SED fitting is performed with a hybrid strategy that combines the database method and the simulated

Table 2. Disk parameter values of the best-fit SED model.

R_{in} [AU]	R_{out} [AU]	p	β	h_{100} [AU]	m_{disk} [$10^{-5}\,M_{\odot}$]	m_{disk} [$M_{\oplus}$]	i [°]
0.023	100	1.136	1.317	17.42	9.06	30.2	58

Notes. For the photosphere, the values of set 2 of Table 1 were used. See Sect. A for confidence intervals of the disk parameters.

annealing (SA) algorithm (Liu et al. 2013). We first run a large grid of disk models with a broad range of disk parameters. Then SA is used to improve upon the results returned by the model grid and to calculate local confidence intervals. The best-fit model is shown in Fig. 1 and the corresponding disk parameter values are listed in Table 2. The best-fit model is not a unique solution due to model degeneracies between different parameters, for example m_{disk}/R_{out}. We therefore conduct a Bayesian analysis to estimate the validity range for each parameter (Pinte et al. 2008). We find that the best-fit and the most probable values (cf. Sect. A) agree well with each other, in particular the disk mass, which demonstrates that the modeling efforts place good constraints on the mass and structure of the disk of OTS 44. We note that strong grain growth would remain undetected in our data (≤160 μm) and could affect m_{disk}. The values of most disk parameters derived here are largely consistent with the results of Harvey et al. (2012, R_{in} = 0.01 AU, $m_{disk} = 5.0 \times 10^{-5}\,M_{\odot}$, β = 1.15, h_{100} = 15 AU, i = 60°), who used a coarser grid resolution and slighlty different dust properties and photospheric parameters. An SED model by Bonnefoy et al. (2013) aimed at understanding whether the disk could create a near-IR excess that would bias the temperature estimate, showed that this is not the case.

5. Paschen β and Hα emission

We discover a strong and broad Paschen β (Pa β) emission line in our near-IR SINFONI spectra of OTS 44 (Fig. 2). Furthermore, a prominent Hα emission line is visible in the optical spectrum of Luhman (2007, see Fig. 2). Both of these Hydrogen emission lines exhibit a broad profile with velocities of ±200 km s^{-1}or more. We investigate the properties and origin of these lines through a line profile analysis. We determine the equivalent width (EW) by directly integrating the flux within the line region and the EW errors following Sembach & Savage (1992). Furthermore, we measure the line center and full width at half maximum (FWHM) based on a Gaussian fit to the profiles. Table 3 lists the results.

The Hα line has a symmetrically shaped profile with an EW of −141 Å, demonstrating that OTS 44 is actively accreting (e.g. Barrado & Martin 2003). The line appears to be blueshifted with its center located at −30 km s^{-1}. Higher resolution spectroscopy is needed to determine whether this shift is real.

The shape of the Pa β line appears to be slightly asymmetric, with the red wing being more pronounced. The profile is significantly variable between the two observing epochs separated by a few days. We measure an EW of −6.7 and −4.2 Å for the spectra from December 14 and 21, respectively. The line has a peak at redshifted velocities at about 40−50 km s^{-1}. We see a redshift of similar order also in photospheric lines of OTS 44. While the Pa β emission of T Tauri stars is mostly attributed to magnetospheric accretion and winds (e.g., Rigliaco et al. 2012), there is observational evidence that part of the Pa β emission, in particular the broad line wings, can be formed by other processes, such as outflows (e.g., Whelan et al. 2004). We conducted

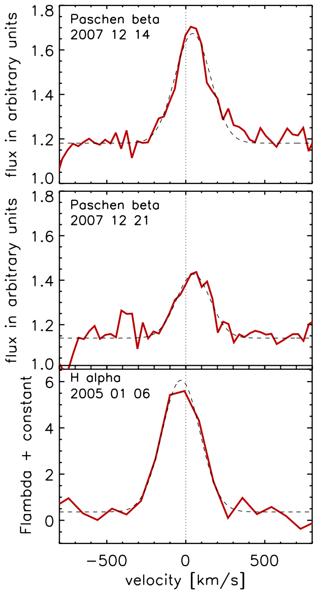

Fig. 2. Pa β emission of OTS 44 in SINFONI/VLT spectra and Hα emission of OTS 44 based on a spectrum from Luhman (2007). The dashed lines are Gaussian fits to the profiles.

Table 3. Observed emission lines of OTS 44.

Line	Date	V_{center} [km s^{-1}]	*FWHM* [km s^{-1}]	*EW* [Å]
Hα	2005 01 06	−30	283	−141 ± 14
Pa β	2007 12 14	+44	265	−6.7 ± 0.3
Pa β	2007 12 21	+48	251	−4.2 ± 0.3

a spectro-astrometric analysis of the Pa β line in the SINFONI 3D cube data to locate the formation site of this emission. We find no spectro-astrometric signal in this line that exceeds 5 mas (0.8 AU).

Mass accretion rate. We determine the mass accretion rate of OTS 44 based on the Hα line by assuming that the Hα emission is entirely formed by accretion processes. For this purpose, we calculate the Hα line luminosity from the Hα EW using broad-band photometry and converte it into an accretion luminosity by applying the empirical relation of Fang et al. (2009, cf. also Joergens et al. 2012b). We use a dereddened R-band magnitude, a distance of 162.5 pc, the set 2 parameters (Table 1) for the extinction and for calculating a radius via the Stefan-Boltzmann law, and a mass of 11.5 M_{Jup}, which is an intermediate value of the estimated range of 6−17 M_{Jup} (Luhman et al. 2005b; Bonnefoy et al. 2013). We derive an Hα line luminosity of $6.9^{+1.4}_{-1.2} \times 10^{-7}\,L_{\odot}$, an accretion luminosity of $3.7^{+17.4}_{-3.1} \times 10^{-6}\,L_{\odot}$ (0.15% of L_*), and a mass accretion rate of $7.6^{+36}_{-6.4} \times 10^{-12}\,M_{\odot}\,yr^{-1}$. We take into account errors in EW, R_{mag}, and in the empirical relation. We furthermore attempt to estimate the mass accretion rate based on the Pa β line by using the empirical relation of Rigliaco et al. (2012), a dereddened J-band magnitude, and again set 2 of Table 1. This yields a mass rate that is two orders of magnitude higher than that derived from Hα, namely $1.7 \times 10^{-9}\,M_{\odot}\,yr^{-1}$ for epoch 1 (December 14) and $8.5 \times 10^{-10}\,M_{\odot}\,yr^{-1}$ for epoch 2 (December 21). This descrepancy lets us speculate that part of the Pa β line might come from a different origin than accretion.

6. Conclusions

We have discovered strong, broad, and variable Pa β emission of the young very low-mass brown dwarf OTS 44 (M9.5) in VLT/SINFONI spectra, which is evidence for active accretion

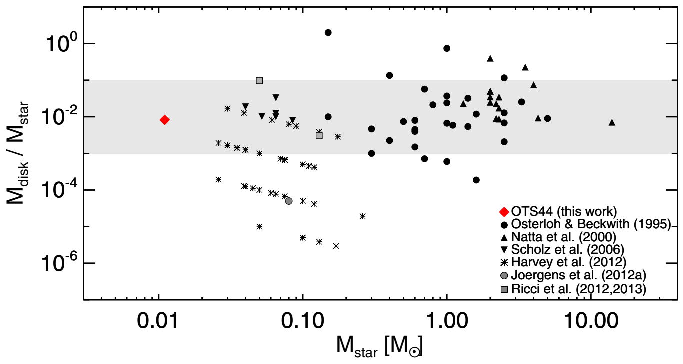

Fig. 3. Relative disk mass versus central mass of stars and brown dwarfs including OTS 44 (red diamond). We note that for ρ Oph102 we use $M_* = 0.13\,M_\odot$ (M5.5, Luhman, priv. comm.), different from Ricci et al. (2012, 0.06 $M_\odot$).

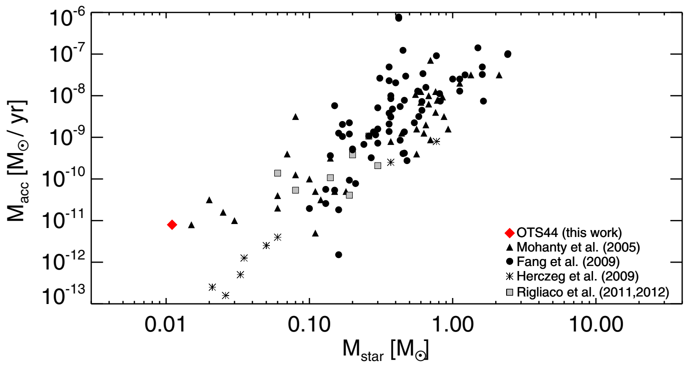

Fig. 4. Mass accretion rate versus central mass of stars and brown dwarfs including OTS 44 (red diamond).

at the planetary border. We determined the properties of the disk that surrounds OTS 44 through MC3D radiative transfer modeling of flux measurements from the optical to the far-IR (*Herschel*). We found that OTS 44 has a highly flared disk ($\beta > 1.2$) with a mass of $9.1^{+1.7}_{-5.5} \times 10^{-5}\,M_\odot$, i.e. about 0.1 $M_{\rm Jup}$ or 30 $M_{\rm Earth}$. We also investigated the Hα line of OTS 44 in a spectrum from Luhman (2007) and found strong Hα emission with an EW of -141 Å indicative of active accretion. Both the Paβ and Hα emission lines of OTS 44 have broad profiles with the wings extending to velocities of about ± 200 km s^{-1}. The Paβ emission is significantly variable on timescales of a few days, indicating variability in accretion-related processes of OTS 44. We estimated the mass accretion rate of OTS 44 to $7.6^{+36}_{-6.4} \times 10^{-12}\,M_\odot\,{\rm yr}^{-1}$ by using the Hα line. A mass accretion rate based on the Paβ line gives a significantly higher value, and we speculate that part of the Paβ emission might come from other processes related to accretion, such as outflows. Furthermore, in the course of studying OTS 44, we fitted a photospheric BT-Settl model to its optical and near-IR SED and derived a lower effective temperature and higher extinction than was previously found (Luhman 2007).

We have presented the first detection of Paβ emission for an object at the deuterium-burning limit. Our analysis of Paβ and Hα emission of OTS 44 demonstrates that objects of a few Jupiter masses can be active accretors. Furthermore, OTS 44 is the lowest-mass object to date for which the disk mass is determined based on far-IR data. Our detections therefore extend the exploration of disks and accretion during the T Tauri phase down to the planetary mass regime. Plotting the relative disk masses of stars and brown dwarfs including OTS 44 (Fig. 3) shows that the ratio of the disk-to-central-mass of about 10^{-2} found for objects between 0.03 $M_\odot$ and 14 $M_\odot$ is also valid for OTS 44 at a mass of about 0.01 $M_\odot$. Furthermore, the mass accretion rate of OTS 44 is consistent with a decreasing trend from stars of several solar masses to brown dwarfs down to 0.01 $M_\odot$ (Fig. 4). It is also obvious from this figure that OTS 44 has a relatively high mass accretion rate considering its small mass. These observations show that the processes that accompany canonical star formation, disks and accretion, are present down to a central mass of a few Jupiter masses. OTS 44 plays a key role in the study of disk evolution and accretion at an extremely low mass and, therefore, in constraining the minimum mass that star formation can produce. It will be the target of our future observational efforts.

Acknowledgements. We thank K. Luhman for providing the optical spectrum of OTS 44 and related information, C. Dumas and A.-M. Lagrange for help with the SINFONI data reduction, the ESO staff at Paranal for executing the SINFONI observations in service mode, and the anonymous referee for very helpful comments. This work made use of the NIST database (Kramida et al. 2012) and VOSA (Bayo et al. 2008). MB acknowledges funding from Agence Nationale pour la Recherche, France through grant ANR10-BLANC0504-01.

References

Allard, F., Homeier, D., Freytag, B., & Sharp, C. M. 2012, in EAS Pub. Ser. 57, eds. C. Reyle, C. Charbonnel, & M. Schultheis, 3
Bacciotti, F., Whelan, E. T., Alcalá, J. M., et al. 2011, ApJ, 737, L26
Barrado y Navascués, D., & Martín, E. L. 2003, AJ, 126, 2997
Bayo, A., Rodrigo, C., Barrado Y Navascués, D., et al. 2008, A&A, 492, 277
Bayo, A., Barrado, D., Huelamo, N., et al. 2012, A&A, 547, A80
Bonnefoy, M., Chauvin, G., Lagrange, A.-M., et al. 2013, A&A, in press, DOI: 10.1051/0004-6361/201118270
Chiang, E. I., & Goldreich, P. 1997, ApJ, 490, 368
Fang, M., van Boekel, R., Wang, W., et al. 2009, A&A, 504, 461
Harvey, P. M., Henning, Th., Liu, Y., et al. 2012, ApJ, 755, 67
Herczeg, G. J., Cruz, K. L., & Hillenbrand, L. A. 2009, ApJ, 696, 1589
Inutsuka, S., & Miyama, S. M. 1992, ApJ, 388, 392
Joergens, V. 2006, A&A, 448, 655
Joergens, V., Pohl, A., Sicilar-Aguilar, A., & Henning, Th. 2012a, A&A, 543, A151
Joergens, V., Kopytova, T., & Pohl, A. 2012b, A&A, 548, A124
Liu, Y., Madlener, D., Wolf, S., & Wang, H.-C. 2013, Res. Astron. Astrophys., 13, 420
Luhman, K. L. 2007, ApJS, 173, 104
Luhman, K. L., Peterson, D. E., & Megeath, S. T. 2004, ApJ, 617, 565
Luhman, K. L., Adame, L., D'Alessio, P., et al. 2005a, ApJ, 635, L93
Luhman, K. L., D'Alessio, P., Calvet, N., et al. 2005b, ApJ, 620, L51
Luhman, K. L., Allen, L. E., Allen, P. R., et al. 2008, ApJ, 675, 1375
Machida, M. N., Inutsuka, S., & Matsumoto, T. 2009, ApJ, 699, L157
Mohanty, S., Jayawardhana, R., & Basri, G. 2005, ApJ, 626, 498
Monin, J.-L., Whelan, E. T., Lefloch, B., Dougados, C., & Alves de Oliveira, C. 2013, A&A, 551, L1
Natta, A., Grinin, V., & Mannings, V. 2000, Protostars and Planets IV (Tucson: University of Arizona Press), 559
Oasa, Y., Tamura, M., & Sugitani, K. 1999, ApJ, 526, 336
Osterloh, M., & Beckwith, S. V. W. 1995, ApJ, 439, 288
Phan-Bao, N., Riaz, B., Lee, C.-F., et al. 2008, ApJ, 689, L141
Pinte, C., Padgett, D. L., Ménard, F., et al. 2008, A&A, 489, 633
Ricci, L., Testi, L., Natta, A., Scholz, A., & de Gregorio-Monsalvo, I. 2012, ApJ, 761, L20
Ricci, L., Isella, A., Carpenter, J. M., & Testi, L. 2013, ApJ, 764, L27
Rigliaco, E., Natta, A., Randich, S., et al. 2011, A&A, 526, L6
Rigliaco, E., Natta, A., Testi, L., et al. 2012, A&A, 548, A56
Scholz, A., Jayawardhana, R., & Wood, K. 2006, ApJ, 645, 1498
Sembach, K. R., & Savage, B. D. 1992, ApJS, 83, 147
Whelan, E. T., Ray, T. P., & Davis, C. J. 2004, A&A, 417, 247
Whelan, E. T., Ray, T. P., Bacciotti, F., et al. 2005, Nature, 435, 652
Wolf, S. 2003, Comp. Phys. Comm., 150, 99
Wolf, S., Padgett, D. L., & Stapelfeldt, K. R. 2003, ApJ, 588, 373

Page 5 is available in the electronic edition of the journal at http://www.aanda.org

Appendix A: Bayesian probability analysis

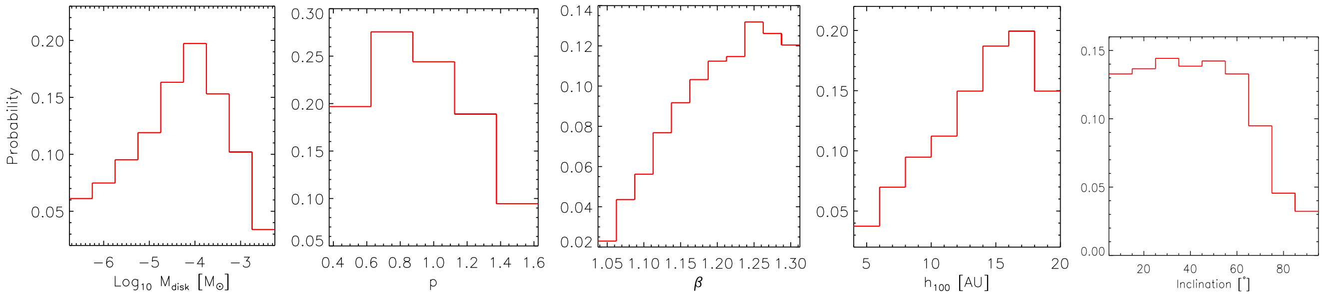

Fig. A.1. Bayesian probability distributions of selected disk parameters.

Table A.1. Confidence intervals of the disk parameter values of OTS 44.

Parameter	Best model	Valid range
$R_{\rm in}$ [AU]	$0.023^{+0.018}_{-0.013}$	0.01–0.04
$R_{\rm out}$ [AU]	100	fixed
p	$1.136^{+0.051}_{-0.025}$	0.62–1.27
β	$1.317^{+0.017}_{-0.042}$	1.16–1.32
h_{100} [AU]	$17.42^{+0.68}_{-2.55}$	9.0–18.5
$m_{\rm disk}$ [$10^{-5}\ M_\odot$]	$9.06^{+1.72}_{-5.46}$	0.32–56.2
i [°]	58^{+6}_{-9}	18–65

Notes. Parameter values of the best-fit SED model with local errors and the valid ranges for each parameter. The local error is deduced based on simulated annealing by probing the direct environment of the best fit with a Markov chain. The valid range for each parameter gives a 68% confidence interval based on the Bayesian probability distribution, as shown in Fig. A.1.